

Strain-Induced Decoupling Drives Gold-Assisted Exfoliation of Large-Area Monolayer 2D Crystals

Jakob Ziewer,* Abyay Ghosh, Michaela Hanušová, Luka Pirker, Otakar Frank, Matěj Velický, Myrta Grüning, and Fumin Huang*

Gold-assisted exfoliation (GAE) is a groundbreaking mechanical exfoliation technique that produces centimeter-scale single-crystal monolayers of 2D materials. Such large, high-quality films offer unparalleled advantages over the micron-sized flakes typically produced by conventional exfoliation techniques, significantly accelerating the research and technological advancements in the field of 2D materials. Despite its wide applications, the fundamental mechanism of GAE remains poorly understood. In this study, using MoS₂ on Au as a model system, ultra-low frequency Raman spectroscopy is employed to elucidate how the interlayer interactions within MoS₂ crystals are impacted by the gold substrate. The results reveal that the coupling at the first MoS₂-MoS₂ interface between the adhered layer on the gold substrate and the adjacent layer is substantially weakened, with the binding force being reduced to nearly zero. This renders the first interface the weakest point in the system, thereby the crystal preferentially cleaves at this junction, generating large-area monolayers with sizes comparable to the parent crystal. Biaxial strain in the adhered layer, induced by the gold substrate, is identified as the driving factor for the decoupling effect. The strain-induced decoupling effect is established as the primary mechanism of GAE, which can also play a significant role in general mechanical exfoliations.

1. Introduction

Gold-assisted exfoliation (GAE) is a groundbreaking mechanical exfoliation technique capable of producing centimeter-scale single-crystal monolayers of a diverse range of 2D materials.^[1–4] It expands the exfoliated film area by several orders of magnitude compared to the conventional technique using scotch tape and SiO₂ substrates.^[5] Although bottom-up synthesis methods, such as physical vapor deposition and chemical vapor deposition, can yield wafer-scale monolayers,^[6–8] their quality is often compromised by defects and polycrystallinity.^[9,10] By contrast, GAE produces pristine monolayer crystals of superior quality.^[11] Combining scalability and excellent material quality, GAE provides unprecedented opportunities for advanced research and technological development in the field of 2D materials, becoming central to the construction of a wide variety of structures, including free-standing monolayers, heterostructures, and moiré superlattices.^[12–15]

The GAE technique is broadly applicable to 2D materials containing sulfur (S), selenium (Se), or tellurium (Te), such as transition metal dichalcogenides (TMDCs) including MoS₂, WS₂, MoSe₂, WSe₂, MoTe₂, WTe₂, and various other chalcogenides like InSe, GaSe, In₂Se₃, Cr₂Ge₂Te₆, and Fe₃GeTe₂.^[1,2] It has also been applied to a few non-chalcogenide 2D materials, such as graphene, hexagonal boron nitride (hBN), black phosphorus, CrSBr, and CrCl₃.^[2,13,16,17] To date, more than fifty layered materials have been successfully exfoliated with GAE.^[2,18] Recently, the technique has been extended to alternative metals including Ag, Pd, Cu, Ni, and Co.^[19–21]

Despite its extensive use and significant impacts in the field of 2D materials, the fundamental mechanism of GAE and, more generally, metal-assisted exfoliation, remains poorly understood. Adhesion between 2D crystals and the gold substrate has been proposed as a key factor.^[1,2,22] It is assumed for the large-area exfoliation to take place, the adhesion of the 2D crystal to the substrate needs to exceed the interlayer van der Waals (vdW) force within the 2D crystal.^[1,2] However, this fails to explain why GAE predominantly produces large-area monolayers with near-unity yield, instead of randomly generating flakes of various

J. Ziewer, A. Ghosh, M. Grüning, F. Huang
Centre for Quantum Materials and Technologies
School of Mathematics and Physics
Queen's University Belfast
University Road, Belfast BT7 1NN, UK
E-mail: jziewer01@qub.ac.uk; f.huang@qub.ac.uk

M. Hanušová, L. Pirker, O. Frank, M. Velický
J. Heyrovský Institute of Physical Chemistry
Czech Academy of Sciences
Dolejškova 2155/3, Prague 18223, Czech Republic
M. Hanušová
Faculty of Chemical Engineering
University of Chemistry and Technology
Prague Technická 5, Prague 6 16628, Czech Republic

 The ORCID identification number(s) for the author(s) of this article can be found under <https://doi.org/10.1002/adma.202419184>

© 2025 The Author(s). Advanced Materials published by Wiley-VCH GmbH. This is an open access article under the terms of the [Creative Commons Attribution](#) License, which permits use, distribution and reproduction in any medium, provided the original work is properly cited.

DOI: 10.1002/adma.202419184

thicknesses as is the case for the scotch tape/SiO₂ method. The substrate-induced strain has been hypothesized as a potential driver, weakening the coupling at the first interface between the adhered layer and the adjacent layer, favoring monolayer exfoliation.^[3,22–24] However, these are only speculations. To date, solid experimental evidence supporting this hypothesis has been lacking, leaving critical aspects of the mechanism unresolved.

In this work, we present compelling experimental evidence to reveal the fundamental mechanism of GAE. Using MoS₂ on gold as a model system,^[1–3] we characterized the force constants at the first MoS₂-MoS₂ interface, i.e., the interface between the bottommost layer adhered to the gold substrate and the adjacent upper layer, through ultra-low frequency (ULF) Raman spectroscopy.^[25–28] Our findings reveal that the coupling at the first interface is significantly weakened during the exfoliation process, with the degree of decoupling depending on crystal thickness. For bilayers, the coupling is weakened by ≈20%, which increases to ≈50% for tetralayers, and ≈100% for crystals thicker than five layers. These results indicate that the first interface is the weakest point in the system. Therefore, MoS₂ crystals preferentially cleave at this interface, generating large-area monolayers on the gold substrate.

This finding is further supported by the observation of micron-sized bubbles in annealed samples of MoS₂ on Au. When samples of MoS₂ on Au were annealed at 200 °C, micron-sized bubbles were observed forming in flakes thicker than three layers but not in thin flakes of 1–3 layers. When the samples were further annealed at an elevated temperature of 400 °C, the bubbles burst, and all the exposed surfaces were shown to be monolayers. This provides direct experimental evidence unambiguously confirming that the first MoS₂-MoS₂ interface is the weakest point in the system and that MoS₂ crystals preferentially break at this interface. Biaxial strain in the adhered layer, induced by the gold substrate, is identified to be the primary driver of the decoupling effect. Density functional theory (DFT) simulations reveal that when the strain in the adhered layer and the crystal thickness exceed specific thresholds, monolayer exfoliation becomes energetically favorable.

2. Results and Discussions

2.1. Sample Fabrication and Thickness Characterization

The processes of GAE have been described in a previous study,^[1] briefly summarized here: MoS₂ crystals are cleaved just prior to exfoliation to minimize contamination; the cleaved surface is then pressed onto a freshly prepared Au substrate and lifted off, resulting in large-area monolayers adhered to the Au substrate. A range of samples were prepared on thin Au films of various thicknesses (2, 5, and 10 nm) as well as on commercially purchased template-stripped (TS) Au films of 100 nm. All thin Au films (unless otherwise stated) were deposited on a SiO₂ (100 nm)/Si substrate (referred to as SiO₂ hereafter) with a 1 nm Ti adhesion layer through magnetron sputtering. For all Au samples, the exfoliated MoS₂ crystals are predominantly monolayers exceeding 1 μm in lateral dimension (limited by parent crystal size), as shown in Figure 1a and Figure S1 (Supporting Information). Besides the monolayers, there are usually some scarcely distributed multilayers (Figure 1b). For comparison, we also prepared MoS₂ crystals

on bare SiO₂ substrates as reference samples, which comprise small flakes (<20 μm) of various thicknesses (Figure 1c). More details of sample fabrication are described in Methods and in previous publications.^[1,29]

The thickness of MoS₂ layers is determined through multiple characterizations, including optical contrast, Raman, and AFM measurements. For example, the intensity ratios between the Raman modes (E_{2g}^1 and A_{1g} modes, using the bulk notation) of MoS₂ and the underlying Si substrate (520.7 cm⁻¹ peak) are shown to be quasi-linearly proportional to the layer number (Figure 1d,e), which can be used to accurately determine the thickness of MoS₂.^[30] This, corroborated with optical contrast, ULF Raman, and AFM measurements (Figure S2, Supporting Information), allows us to accurately identify 1–10 layer MoS₂ on Au and SiO₂.

2.2. High-Frequency Raman Spectra: Strain in the Adhered Layer

We first investigated the high-frequency Raman spectra of MoS₂. Figure 2 shows examples of the high-frequency Raman spectra of MoS₂ on 10 nm Au (Figure 2a) and SiO₂ (Figure 2b) substrates. The high-frequency Raman spectra show two main vibration modes, E_{2g}^1 mode (in-plane) and A_{1g} mode (out-of-plane). The frequency and intensity of both modes are thickness-dependent. For MoS₂ films on SiO₂, both the E_{2g}^1 mode and the A_{1g} mode displays a single peak. The A_{1g} mode upshifts while the E_{2g}^1 mode downshifts with increasing thickness, in agreement with prior literature.^[31]

For MoS₂ on Au, the spectra are notably different. The E_{2g}^1 mode of a monolayer displays a single peak at 380 cm⁻¹ (Figure 2d), which is downshifted by 6 cm⁻¹ with respect to its SiO₂ counterpart (386 cm⁻¹). The downshift of the E_{2g}^1 mode indicates the presence of a biaxial strain in the monolayer.^[29,32] Based on the frequency shift, the mean strain is estimated to be 1.1% using a literature-averaged Grüneisen parameters of 0.71 (using the formula $\epsilon = \frac{\Delta\omega}{2\gamma\omega_0}$, $\Delta\omega$ is frequency shift, ω_0 is the frequency at zero strain, and γ is the Grüneisen parameter),^[32–34] close to the 1.2% reported previously.^[29]

The E_{2g}^1 mode of 2–4L MoS₂ on Au shows splitting, which can be fitted with two Lorentzian peaks (Figure 2d). The peak positions of Raman modes averaged from several spectra are presented in Figure 2c. As seen from Figure 2c,d, the low-frequency peaks of the MoS₂ E_{2g}^1 doublets on Au (denoted as E(L) in Figure 2c) remain at ≈380 cm⁻¹ for the bilayer, trilayer, and tetralayer, closely matching that of the monolayer. This suggests that the E(L) peak originates from the bottom strained layer adhered to the Au substrate. On the other hand, the high-frequency components of the E_{2g}^1 doublets match those on SiO₂, implying that they originate from the top layer(s), which are little affected by the strained bottom layer. This indicates that the biaxial strain is mostly localized in the bottom adhered layer with little transfer to subsequent layers, consistent with theoretical simulations.^[24,35] These results are observed on all Au samples, with some variance in the shift of the monolayer E(L) peaks, with the lowest being (377.8 ± 0.1) cm⁻¹ for 2 nm Au samples and the highest being (380.0 ± 0.1) cm⁻¹ for 5 nm Au samples, indicating a strain ranging from roughly 1.5% to 1.1%.

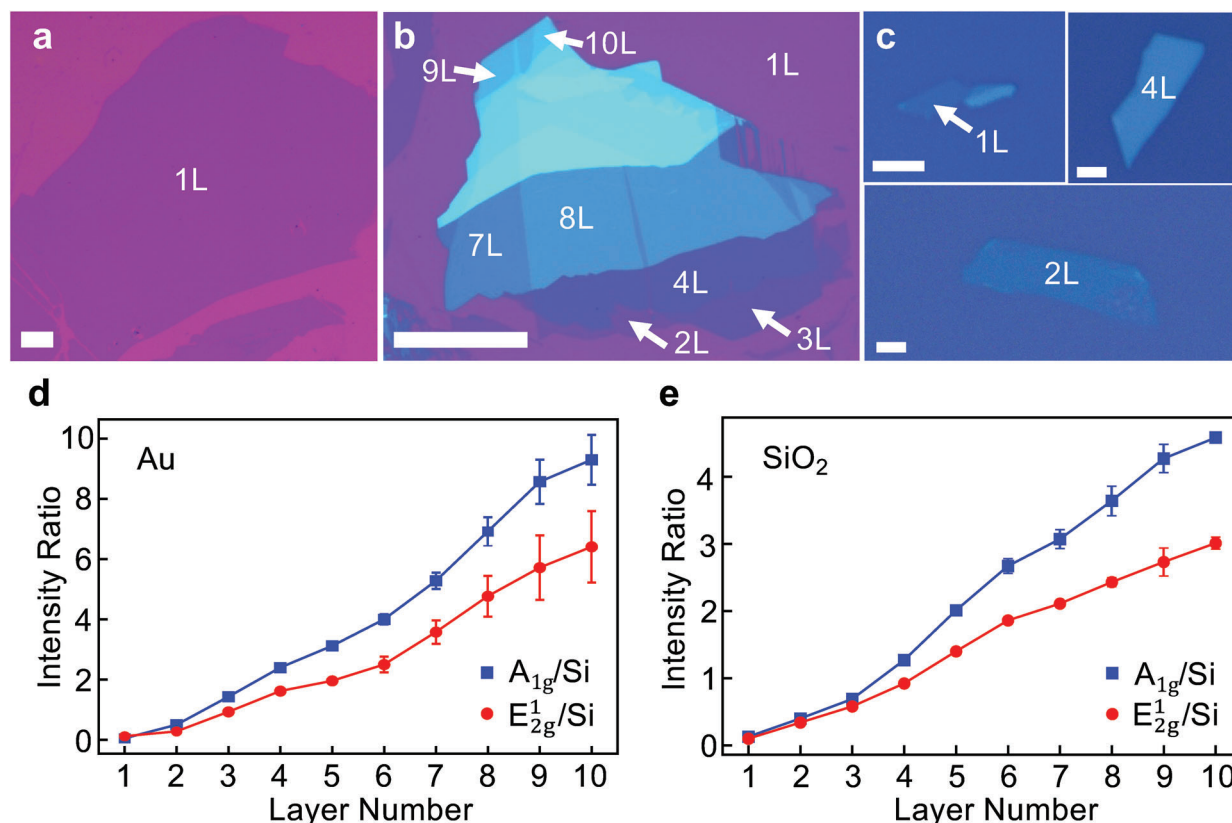


Figure 1. Optical images of MoS₂ and thickness characterization. Optical images of large-area monolayer a) and few-layer b) MoS₂ exfoliated on a 10 nm Au substrate. Scale bars: 100 μ m. c) Optical images of MoS₂ exfoliated on a SiO₂ (100 nm)/Si substrate. All scale bars are 2 μ m. d,e) Raman intensity ratios of the MoS₂ E_{2g}^1 and A_{1g} peaks to the Si peak at 520.7 cm^{-1} for 1–10L MoS₂ on a 10 nm Au substrate (d) and a SiO₂ (100 nm)/Si substrate (e).

Unlike the E_{2g}^1 mode, the A_{1g} mode of monolayer MoS₂ on Au shows a distinct doublet, with one peak at 396.0 cm^{-1} and the other at 404.5 cm^{-1} . The high frequency peak (404.5 cm^{-1}) closely matches that of SiO₂. The appearance of the 396.0 cm^{-1} peak is attributed to doping effects,^[29,36] suggesting a doped-electron concentration of $3.6 \times 10^{13} \text{ cm}^{-2}$ (equivalent of 0.033 extra electrons per unit cell).^[37] The E_{2g}^1 mode is sensitive to in-plane strain but less to doping, while the A_{1g} mode is sensitive to doping but not significantly to strain. For the strain and doping observed here the covariance of the E_{2g}^1 and A_{1g} modes is negligible, and shifts in each can be taken to arise solely from strain or doping, respectively.^[36]

The intensities of both the E(L) peak and the A(L) peak (the low-frequency components of the E_{2g}^1 and A_{1g} modes, respectively) decrease with thickness (Figure 2d). This is because the light emission from the adhered bottom monolayer is damped due to absorption by the top layer(s), which becomes stronger with increasing thickness. Furthermore, as thickness increases, the top layer(s) emission becomes stronger, obscuring the signals of the bottom adhered layer. These factors lead to the diminished intensities of the E(L) and A(L) modes with increasing thickness. The E(L) mode is visible up to four layers, while the A(L) mode is only clearly visible on monolayers. Very weak signals of the A(L) mode can be identified in 2–3L flakes, as indicated by the little humps in the spectra, which are not present for SiO₂ samples

(since the intensities of the A(L) mode in 2L and 3L flakes are very weak, the fitting results are not reliable, and only the monolayer peak position is presented in Figure 2c). It is not exactly clear why the intensities of the two modes attenuate differently. We suspect this might be related to the nature of the in-plane and out-of-plane vibrations of the E(L) mode and the A(L) mode, respectively (see Supporting Information for more detailed discussion).

2.3. ULF Raman: Shear and Breathing Modes

Figure 3 shows the ULF Raman spectra of 1–10L MoS₂ on 10 nm Au and SiO₂ substrates. The weak interlayer interactions within 2D materials often manifest as ULF Raman modes with frequencies below 100 cm^{-1} .^[25–28] Such modes normally consist of two types of vibrations: the shear modes for which individual layers move relative to each other parallel to the layer plane (Figure 3a) and the breathing modes for which the layers move perpendicularly to the layer plane (Figure 3b).

For MoS₂ on SiO₂, both the first-order shear modes (S1) and the first-order breathing modes (B1) are strong and clearly visible (Figure 3c). The S1 mode upshifts while the B1 mode downshifts with the number of layers, consistent with the literature.^[25–27] The spectra on Au are distinctly different. The S1 modes on Au

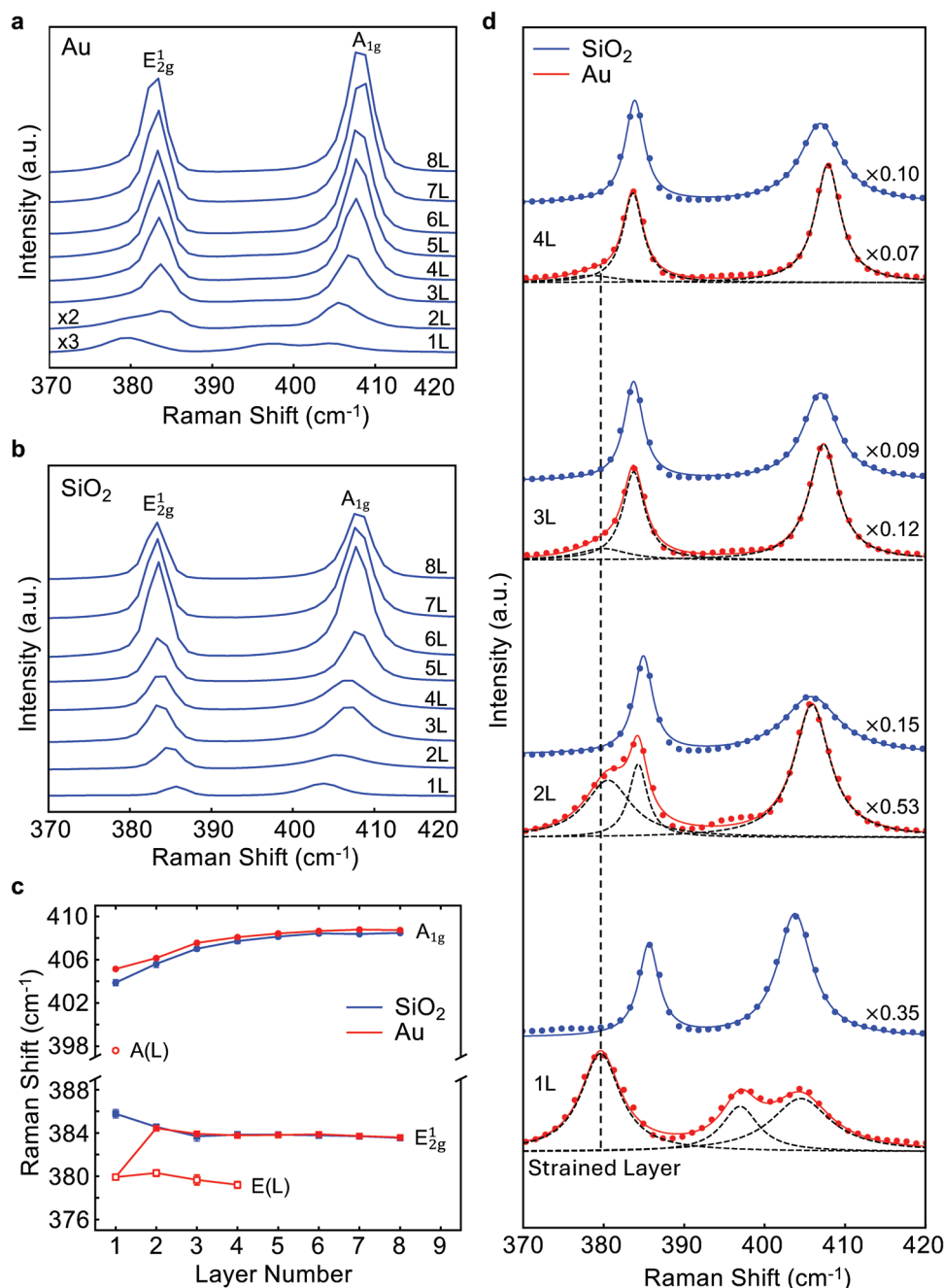


Figure 2. High-frequency Raman spectra of MoS₂. Raman spectra of 1–8L MoS₂ on a) 10 nm Au and b) SiO₂ substrates. c) Peak frequencies of the Raman modes. The E_{2g}¹ modes of 2–4L MoS₂ on Au consist of two peaks, a low-frequency peak E(L) ≈ 380 cm^{−1}, close to the E_{2g}¹ mode of the monolayer on Au, and a high-frequency peak matching that on SiO₂, suggesting that E(L) originates from the strained bottom layer, and the high-frequency peak originates from the top unstrained layer(s). d) Comparison of the Raman spectra of 1–4L MoS₂ on SiO₂ and Au substrates. Dashed lines: Lorentzian fitting of Raman peaks. The vertical line marks the peak position of the E_{2g}¹ mode of monolayer on Au. Scaling factors are normalized to the spectrum of monolayer on Au.

are clearly visible, but the B1 modes (marked by triangles) are significantly suppressed (Figure 3d). The exact mechanism for the suppression of the B1 modes is not clear. A similar phenomenon is attributed to the quasi-covalent bonding between MoS₂ and Au.^[38] However, this factor alone cannot explain why the suppression is observed in crystals up to 10 layers and

is selective for the breathing mode. We find that the intensity of the B1 modes varies with Au thickness and appears to be stronger on 2 nm and TS Au than on other Au substrates (Figure S3, Supporting Information). This suggests that there are other mechanisms contributing to the quenching of the B1 modes.

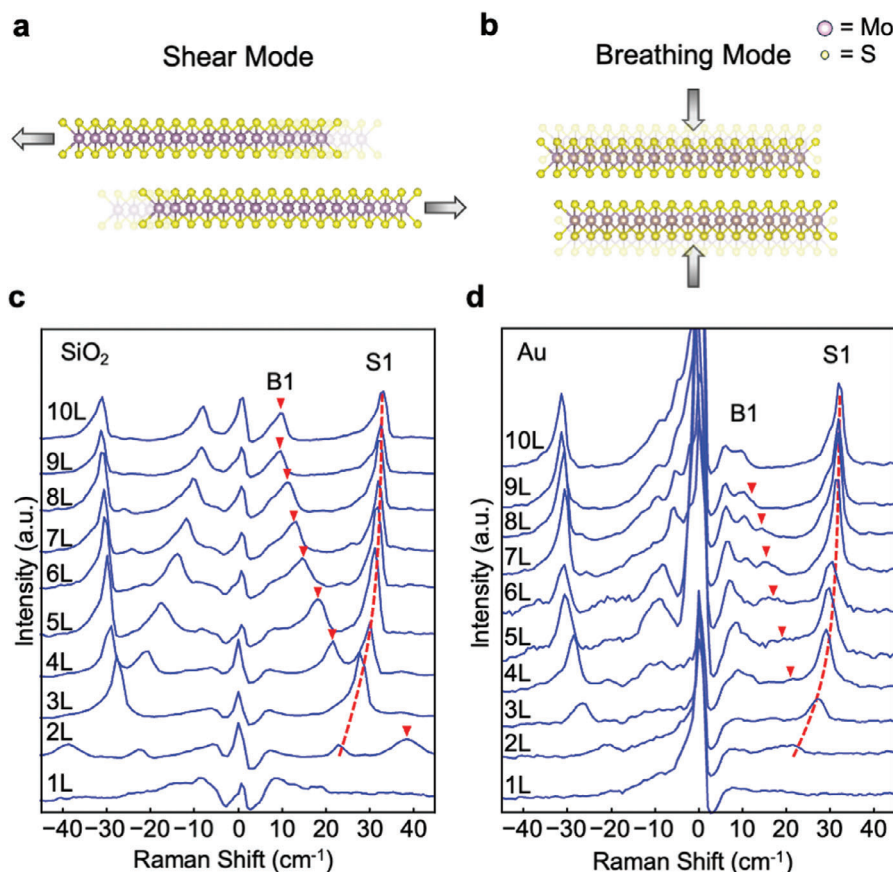


Figure 3. ULF Raman spectra of MoS₂. (a,b) Schematics of the vibrations of shear and breathing modes, respectively. (c,d) Measured ULF Raman spectra of 1–10L MoS₂ on c) SiO₂ and d) 10 nm Au. The dashed lines serve as a guide to the eye for the first-order shear (S1) modes. Triangles mark the locations of the first-order breathing (B1) modes, which are notably suppressed on Au.

The S1 modes and B1 modes of MoS₂ on Au shift with respect to those on SiO₂. To see this more clearly, we plot the Stokes Raman spectra of 2–4L MoS₂ on Au and SiO₂ together in Figure 4a. The S1 modes on Au are downshifted with respect to those on SiO₂. Figure 4b presents the frequencies of S1 and B1 modes of 2–10L MoS₂ on Au and SiO₂. The S1 frequency of bilayer MoS₂ on Au is downshifted by 2.2 cm⁻¹ compared to MoS₂ on SiO₂. The difference decreases with increasing MoS₂ thickness. By contrast, the B1 mode is upshifted for MoS₂ on Au compared to SiO₂.

2.4. Linear Chain Model and Decoupling Effect

To quantify these shifts, we employ a linear chain model (LCM), which can be used to calculate the shear and breathing modes of pristine 2D crystals. The model treats each individual layer as a mass point, and the interaction between adjacent layers is represented by springs with a universal force constant. For an N-layer MoS₂ crystal, the model yields analytical solutions for the S1 and B1 mode frequencies, given by:^[25,27]

$$\omega_{S1} = \sqrt{\frac{K_x}{2\mu\pi^2c^2} \left(1 - \cos\left(\pi\left(\frac{N-1}{N}\right)\right)\right)} \quad (1)$$

$$\omega_{B1} = \sqrt{\frac{K_z}{2\mu\pi^2c^2} \left(1 - \cos\left(\frac{\pi}{N}\right)\right)} \quad (2)$$

where $\omega_{S1/B1}$ are the thickness-dependent frequencies of the S1/B1 modes, respectively, $K_{x/z}$ are the respective interlayer spring constants, c is the speed of light and μ is the mass per unit area of MoS₂.

Both the S1 and B1 modes of MoS₂ on SiO₂ substrates can be well fitted with the LCM model (Figure 4b, filled symbols and dashed blue curves), obtaining a value of $(2.8 \pm 0.1) \times 10^{19} \text{ Nm}^{-3}$ for K_x and a value of $(8.3 \pm 0.1) \times 10^{19} \text{ Nm}^{-3}$ for K_z . These agree well with the literature averages of $(2.8 \pm 0.1) \times 10^{19} \text{ Nm}^{-3}$ and $(8.8 \pm 0.1) \times 10^{19} \text{ Nm}^{-3}$ for K_x and K_z respectively.^[26,27,39] The reliable fit by the LCM model indicates that SiO₂ substrates have minimal impact on the interlayer interaction of the exfoliated MoS₂ layers, confirming that SiO₂ is a good, weakly interacting reference substrate.

The results on Au, however, cannot be fitted with the LCM model with a universal force constant. Naively using this model to fit the data of MoS₂ on Au results in an overestimation of the frequencies of thin crystals ($N \leq 6$) while the frequencies of thicker ones ($N > 6$) are underestimated (dotted red line, Figure 4b). This

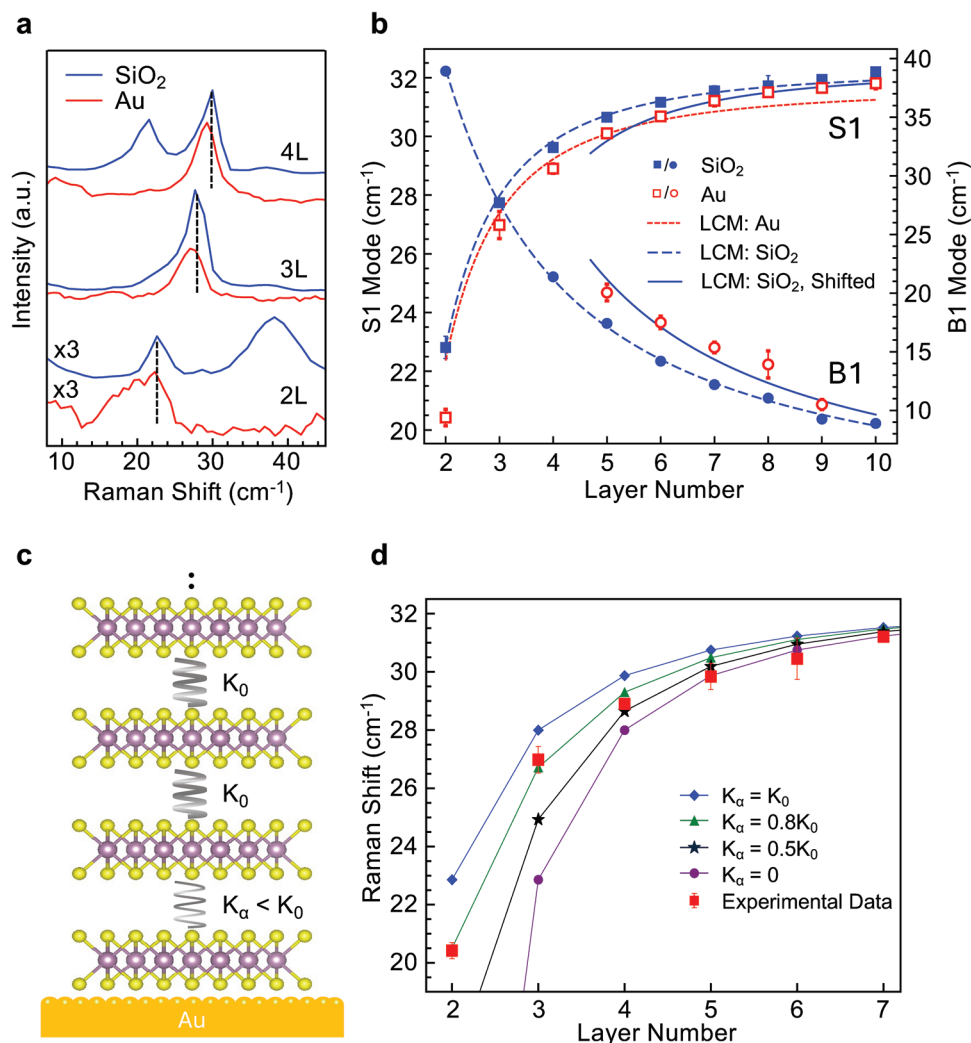


Figure 4. Layer-dependent ULF Raman modes of MoS₂ and LCM fitting. a) ULF Stokes Raman spectra of 2–4L MoS₂ on SiO₂ and 10 nm Au substrates, showing the downshift of the S1 modes on Au with respect to those on SiO₂. Dotted lines mark the peaks of MoS₂ on SiO₂. b) S1 and B1 modes of MoS₂ on SiO₂ (filled symbols) and 10 nm Au (unfilled symbols) substrates. Dashed blue curves: LCM fitting of the S1 and B1 experimental data on SiO₂ substrates. Dotted red curve: LCM fitting of the S1 experimental data on Au substrates, which overestimates the frequencies of thin crystals (< 6 layers) and underestimates those of thicker ones (> 6 layers). Solid blue curves: dashed blue curves shifted to the right by one layer, well matching the data points of ≥ 5L MoS₂ on Au. c) Schematic illustrating a modified linear chain model (mLCM) in which the force constant K_α at the first MoS₂–MoS₂ interface is variable, while the force constants at other interfaces are kept at K_0 , same as that of a pristine MoS₂. d) Solid lines with symbols: S1 modes calculated by mLCM of varying K_α . Comparing the experimental data on Au with the calculated frequencies provides the reduced force constants K_α at the first interface for crystals of different thicknesses. The K_α is $\approx 0.8K_0$ for bilayer and trilayer MoS₂ crystals, $\approx 0.5K_0$ for tetralayer, and nearly zero for crystals thicker than 5 layers, indicating the bottom adhered layer is almost fully decoupled from the top layers.

implies that the force constants are not homogeneous across the interfaces of MoS₂ on Au. The observations that MoS₂ crystals preferentially cleave at the first interface and that the strain is mostly localized to the adhered layer indicate that the force constant at the first interface must be different from those at other interfaces. In light of this, we employ a modified LCM (mLCM) to account for the S1 mode of MoS₂ on Au, where the force constant at the first MoS₂–MoS₂ interface, denoted as K_α , is variable, while those between the remaining layers, K_0 (the force constant of pristine MoS₂), are kept constant, as schematically shown in Figure 4c. The Raman frequency for an N-layer system can then be extracted by solving for the eigenvalues of the correspond-

ing $N \times N$ force constant matrix representing the equations of motion:^[25]

$$\omega_i^2 \tilde{u}_i = \frac{1}{2\pi^2 c^2 \mu} \bar{D} \tilde{u}_i \quad (3)$$

where \bar{D} is the force constant matrix considering only the nearest neighbor interaction and \tilde{u}_i is the i^{th} phonon eigenvector with frequency ω_i .

By calculating the frequencies of the S1 modes at varying K_α values and matching the calculated frequencies with the experimental data on Au, the K_α values of MoS₂ crystals of various

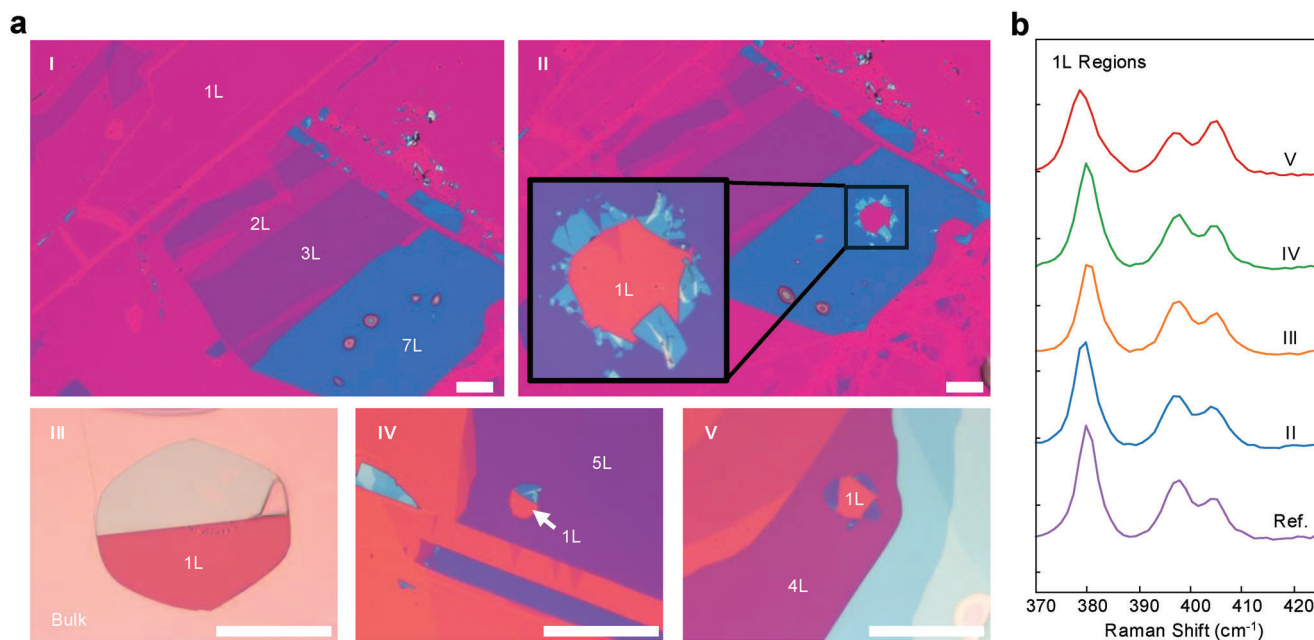


Figure 5. Bubbles in annealed MoS₂ on Au. a) Optical images of MoS₂ on a 10 nm Au substrate after annealing at 200 °C, showing the formation of bubbles in a 7-layer flake, but not in thin flakes of 1–3L (I), and after further annealing at 400 °C, showing the burst of bubbles and the exposed monolayers in flakes thicker than three layers (II–V). All scale bars represent 25 μ m. b) Raman spectra taken at the exposed regions (marked by “1L” in (a)), confirming that the exposed MoS₂ are all monolayers. The reference spectrum of a monolayer MoS₂ on Au, measured on a non-heated sample, is included for comparison.

thicknesses can be deduced. K_a is found to be thickness-dependent, which is $\approx 80\%$ K_0 for bilayers, $\approx 50\%$ K_0 for tetralayers, and $\approx 0\%$ K_0 for crystals thicker than five layers (Figure 4d). A reduced K_a corresponds to weakened coupling at the first interface. The striking finding is that K_a is nearly zero for crystals thicker than five layers. This suggests that the top layers are almost fully decoupled from the adhered bottom layer. In these circumstances, the system of an N-layer crystal is equivalent to a superposition of a monolayer attached to the Au substrate and a decoupled (N – 1) layer sitting on top. Under this assumption, the S1 and B1 modes of a N-layer (N \geq 5) MoS₂ on Au should closely resemble that of a free-standing crystal of (N – 1) layers (since monolayer does not have interlayer modes). To verify this, we shift the LCM fitting curves of the S1 and B1 modes of MoS₂ crystals on SiO₂ to the right by one layer (solid blue curves, Figure 4b) and find that they closely match the data points on Au for MoS₂ thicker than five layers. These phenomena are observed on all Au samples, including 2 nm, 5 nm, and commercially purchased 100 nm TS Au films (Figure S4, Supporting Information), indicating that the observed decoupling effect is universal in GAE.

2.5. Bubbles: Direct Evidence of Decoupling

When MoS₂ on 10 nm Au is annealed at 200 °C in the ambient environment for 5 minutes, bubbles of sizes ranging from a few microns to tens of microns are observed to form in flakes thicker than three layers, but not in thin flakes of 1–3 layers (panel I, Figure 5a). When the samples are further annealed at 400 °C, the bubbles grow and some burst (panel II–V, Figure 5a).

Interestingly, all the exposed surfaces are found to be monolayers (panel II–V, Figure 5a, Figure S5, Supporting Information), as confirmed by the measured Raman spectra, which show a single peak of E_{2g}¹ mode ≈ 380 cm⁻¹ and splitting of A_{1g} modes, matching the spectrum of a reference monolayer on a non-heated Au sample (Figure 5b).

Nanoscale bubbles commonly exist within the weak interfaces of heterostructures or the interfaces between 2D materials and substrates, as the result of tiny air pockets trapped at locations of defects/contaminants. When heated, the air pockets move around and coalesce, forming micron-sized bubbles.^[40,41] Our samples inevitably contain some defects/contaminants (the samples were prepared in the air), so it is normal to have some air pockets. Interestingly, we find micron-sized bubbles only form in flakes thicker than three layers. No microscopic bubbles are observed in 1–3L MoS₂ even after annealing at 400 °C (Figure 5a). This can be understood as follows. For thin flakes of two or three layers, although the interaction at the first MoS₂–MoS₂ interface is weakened, it is only by a small amount ($\approx 20\%$), the layers are still quite strongly bonded, so the movement of trapped air pockets is restricted, unable to form large bubbles. It is even harder for bubbles to form underneath monolayers, as monolayers are strongly pinned on the Au substrate by quasi-covalent force. However, the first interface is significantly weakened for crystals thicker than three layers, as discussed above. As such, when the samples are heated, air pockets can escape into the weakened interface, where they can move and coalesce, forming large bubbles (the top two small bubbles in the 7L flake of panel I merge into a large bubble and burst after further annealing, as shown in panel II, Figure 5a). Since the bubbles form at the

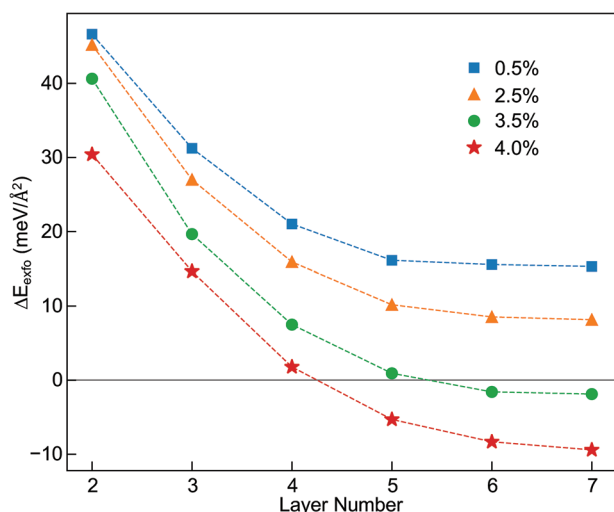


Figure 6. DFT simulation of the exfoliation energy of MoS₂ crystal. Calculated exfoliation energy and its variation with strain and number of layers. Negative/positive values of ΔE_{ext} indicate that monolayer exfoliation is energetically preferable/unfavorable, i.e., for strains of 3.5% and larger, the monolayer is increasingly likely to exfoliate when the whole MoS₂ crystal is thicker than five layers.

weakened interface, a monolayer surface is exposed when they burst. These observations provide direct evidence unambiguously confirming that the first MoS₂-MoS₂ interface is the weakest link in the system, and for crystals thicker than three layers, the adhered bottom layer is significantly decoupled from the top layers, in excellent agreement with the conclusions of the ULF Raman investigation.

2.6. Mechanism of the Decoupling

Strain has been proposed as the possible cause for weakened coupling at the first MoS₂ interface,^[3,22,23] but these are only speculations without solid experimental evidence or details of the weakening mechanism. To shed light on the effects of strain on the exfoliation, we conduct DFT simulations on the energy cost of exfoliation. For a N-layer crystal we compare the energetic cost of two configurations: 1) a system composed of one strained layer and a detached (N – 1) layer crystal free of strain; 2) the whole crystal is strained and allowed to relax. We define the exfoliation energy as

$$\Delta E_{\text{exf}} = \frac{E_{N-1}^0 + E_1}{A} - \frac{E_N}{A} \quad (4)$$

where E_{N-1}^0 is the energy of (N – 1) unstrained layers, E_1 is the energy of a separate strained layer, E_N is the energy of the whole strained stack that has been allowed to relax, and A is the unit-cell area of the strained layer. Negative/positive values of ΔE_{exf} would indicate that monolayer exfoliation is energetically preferable/unfavorable.

The results for various strains and layer numbers of MoS₂ are presented in Figure 6. It shows for relatively small strains, ΔE_{exf} is positive, hence, exfoliation is unfavorable. For strains above 3.5%, ΔE_{exf} crosses the zero axis and becomes negative, indicat-

ing it is energetically favorable for the top stack to be detached from the bottom strained layer. The larger the strain, the thinner the layers for which ΔE_{exf} crosses the zero axis, suggesting it is easier to exfoliate. The results reveal that a certain threshold strain is required to facilitate exfoliation and that the top stack tends to fully decouple from the strained bottom layer when it is thicker than a certain number of layers. Though the simulation is a simplified approximation of the actual experimental configuration, and the calculated threshold strain is larger than the strain measured experimentally, nevertheless, the simulation results provide an insightful picture of the intertwined roles of strain and thickness of MoS₂ crystals, which are qualitatively in agreement with the experimental observations. It is worth noting that the measured strain is an averaged result. At the atomic level, the Au surface is “rough” with protrusions and troughs ranging from angstroms to nanometers.^[1,29] At the protrusion locations, MoS₂ makes good contact with Au, and the strain is high, which could reach or even exceed the criterion strain predicted by the simulations. At the trough regions, the contact is poorer, and the strain is lower.^[29] As such, the measured mean strain could be significantly lower than the maximum strain. It is the high strain at the protrusion locations that plays a central role in driving decoupling, breaking the crystal at the first interface, and initiating exfoliation. Once the exfoliation is initiated, the top crystals can be peeled off, and a large-size monolayer can be exfoliated across the whole Au surface and even across empty holes to create suspended films.^[14]

The simulation does not explicitly reference any specific substrates, implying that the strain-induced decoupling effect is not limited to GAE, which also possibly plays a significant role in general mechanical exfoliations, including the scotch tape/SiO₂ method and metal-assisted exfoliation.

Finally, it is worth discussing the potential contribution of electrostatic force to the decoupling effect. Electrostatic repulsive force due to injected intercalation ions plays a significant role in the electrochemical exfoliation of 2D materials.^[42] However, in GAE, the impact of the electrostatic force due to the doped electrons by the Au substrate is minimal. As shown above, the concentration of doped electrons in the adhered layer is ~0.033 extra electrons per unit cell. Assuming the adjacent upper layer has the same concentration of doped electrons (which is an overestimate), the coulomb repulsive force between the adhered layer and the adjacent layer is 2.3×10^{15} N per unit cell (the interlayer distance is taken as 0.65 nm), the equivalent of a repulsive pressure of 2.5×10^6 Pa, which is only ~0.1% of the interlayer attractive pressure due to the vdW force in MoS₂ (2.4 GPa),^[43] thereby the contribution of electrostatic force to the decoupling effect is negligible. The strain induced by the gold substrate is the primary cause of the decoupling effect in GAE.

3. Conclusions

In summary, using MoS₂ on Au as a model system, we establish that strain-induced decoupling is the primary mechanism of gold-assisted exfoliation. The gold substrate induces a biaxial strain in the adhered MoS₂ layer, which weakens the coupling at the first interface between the adhered layer and the adjacent layer. For MoS₂ crystals thicker than five layers, the coupling at the first MoS₂-MoS₂ interface is reduced almost to zero. This

interface is the weakest link in the system. During exfoliation the 2D crystal preferentially cleaves at this junction, enabling the exfoliation of large-area monolayers. These findings provide valuable insights into the development of advanced exfoliation techniques and have broad implications in diverse research and technological domains.

Previously, it was thought that the adhesion to the substrate must exceed the interlayer vdW force within the 2D crystal to achieve high-yield exfoliation.^[1,2] The findings in this study suggest that this stringent requirement may not be necessary. Instead, the adhesion between the substrate and the 2D crystal need only surpass the weakened binding force at the first interface, which can be considerably weaker than the interlayer vdW force when strain is present. This indicates that even substrates with relatively weak adhesion to 2D materials can facilitate large-area exfoliation, provided sufficient strain is induced in the adhered layer to effectively weaken the interfacial coupling. These findings highlight the potential of substrate engineering, particularly the enhancement of strain in the adhered layer, as a promising strategy to extend high-yield exfoliation techniques to a broader range of substrates and 2D materials, including dielectric substrates and 2D materials that are currently beyond the scope of gold substrates.

Interfaces play an important role in many physical and chemical phenomena (e.g., electrical and thermal conductivity, tunneling effects, charge transfer, and Schottky barriers). As such, the discovery of significant weakening at the first interface of 2D crystals on gold substrates, which may also occur on other strain-inducing substrates, has broad implications across diverse disciplines and technologies, such as nanoelectrodes, field-effect transistors, and photodiodes.

4. Experimental Section

Sample Preparation: All thin-film Au substrates were deposited on 100 nm SiO₂/Si substrates with a 1 nm Ti adhesion layer (except the samples of Figure 2, which were deposited on 300 nm SiO₂/Si substrates with a 3 nm Cr adhesion layer). The SiO₂/Si substrates and adhesion layer had no impact on exfoliation and the results). Prior to exfoliation, SiO₂/Si substrates were subsequently sonicated in acetone, isopropyl alcohol, and deionized water. This was followed by plasma cleaning with a 25%O₂/75%Ar gas mixture or pure O₂. Reference samples were prepared by bringing a MoS₂ (HQ Graphene or Manchester Nanomaterials Ltd.) loaded tape into contact with the freshly cleaned and plasma-activated SiO₂ surface. The samples used for ULF Raman were not heated to avoid introducing strain. For Au samples, bulk MoS₂ was first cleaved with tape. The freshly cleaved crystal surface was then brought into contact with a freshly prepared Au film deposited onto the cleaned SiO₂/Si substrate with an adhesion layer through magnetron sputtering. The Au (Birmingham Metal Ltd. or Micro to Nano Ltd.) and Ti (Testbourne Ltd. or Micro to Nano Ltd.) targets used were of >99.99% purity and the Cr (Micro to Nano Ltd.) was of > 99.95%. For all depositions, the process chamber pressure was better than 9×10^{-9} Torr. For template-stripped samples, pre-prepared chips of 100 nm Au(111) (Platypus Technologies) were peeled from the protective silicon wafer, exposing a fresh, clean Au surface onto which the crystal was exfoliated. In all cases, exfoliation was carried out immediately after surfaces were exposed to air to avoid contamination.

Raman Measurements: ULF Raman measurements were carried out using a home-built ULF Raman apparatus operating at 532 nm in a backscattering configuration. The system was equipped with three BraggGate notch filters (BNF), allowing for ULF measurements down to

7 cm⁻¹. A 100 × objective with N.A. of 0.9 was used for all measurements and the spot size was ≈0.5 μm in diameter. Laser power was kept below 1.5 mW (measured at the sample) to avoid heating. Spectra were measured with an Acton SpectraPro SP-2300 spectrometer (Princeton Instruments) equipped with an iDus 416A CCD (Andor) and an 1800 grooves per mm grating at 500 nm blaze. The spectral resolution of the system was 2.1 cm⁻¹, estimated from the full width at half maximum of the Rayleigh line, and each pixel of the CCD spans 0.8 cm⁻¹. For analysis, all peaks were fitted with a Lorentzian function, and background subtraction was carried out as necessary. The positional error of the peaks was taken to be the error of the fit. The high-frequency Raman spectra were obtained using a WITec alpha300 R Raman spectrometer (Oxford Instruments) with 532 nm excitation wavelength and 1800 grooves per mm grating. The laser was focused through a 100 × objective (Zeiss EC Epiplan-Neofluar) with power set to 0.5 mW to avoid damaging the samples.

AFM Measurements: AFM measurements were taken on an Asylum MFP-3D infinity machine in tapping mode with a 25 nm PPP-EFM tip (Nanosensors). Since the substrate interaction can introduce a large degree of variance in measured thicknesses, where possible, flakes were measured with respect to a monolayer to minimize uncertainty.

DFT Simulations: The plane wave pseudopotential suite QUANTUM ESPRESSO was employed to perform fully self-consistent DFT-based electronic structure calculations by solving the standard Kohn-Sham equations.^[44,45] Ultrasoft pseudopotentials from the PS library were used for Mo and S atoms.^[46] Kinetic-energy cut-offs were fixed to 80 Ry for electronic wave functions after performing rigorous convergence tests. The electronic exchange–correlation was treated under the generalized gradient approximation parametrized by Perdew–Burke–Erzerhof functional.^[47] The Monkhorst–Pack scheme was adopted to sample the Brillouin zone in k-space with a 12 × 12 × 1 grid.^[48] Geometry optimization was performed using the Broyden–Fletcher–Goldfarb–Shanno scheme.^[49] The Convergence threshold of 10⁻¹⁰ and 10⁻⁵ were used on total energy (a.u.) and forces (a.u.) respectively for ionic minimization. The van der Waals interactions between layers were included in the calculation by incorporating the DFT-D3 method.^[50] The multi-layered MoS₂ systems were prepared with the software VESTA.^[51]

Supporting Information

Supporting Information is available from the Wiley Online Library or from the author.

Acknowledgements

J. Z. thanks the UK EPSRC and SFI Centre for Doctoral Training in Photonic Integration and Advanced Data Storage (PIADS) program for the sponsorship of PhD studentship. M.H., L.P., and M.V. acknowledge the funding support by the Czech Science Foundation Project No. GA22-04408S. The support of the European Regional Development Fund, P JAC (project No. CZ.02.01.01/00/22_008/0004558) was also acknowledged.

Conflict of Interest

The authors declare no conflict of interest.

Data Availability Statement

The data that support the findings of this study are available from the corresponding author upon reasonable request.

Keywords

2D materials, decoupling, gold-assisted exfoliation, MoS₂, Raman spectroscopy, strain

Received: December 7, 2024
Revised: February 4, 2025
Published online: February 19, 2025

- [1] M. Velický, G. E. Donnelly, W. R. Hendren, S. McFarland, D. Scullion, W. J. I. DeBenedetti, G. C. Correa, Y. Han, A. J. Wain, M. A. Hines, D. A. Muller, K. S. Novoselov, H. D. Abruña, R. M. Bowman, E. J. G. Santos, F. Huang, *ACS Nano* **2018**, *12*, 10463.
- [2] Y. Huang, Y. H. Pan, R. Yang, L. H. Bao, L. Meng, H. L. Luo, Y. Q. Cai, G. D. Liu, W. J. Zhao, Z. Zhou, Wu, Z. L. Zhu, M. Huang, L. W. Liu, L. Liu, P. Cheng, K. H. Wu, S. B. Tian, C. Z. Gu, Y. G. Shi, Y. F. Guo, Z. G. Cheng, J. P. Hu, L. Zhao, G. H. Yang, E. Sutter, P. Sutter, Y. L. Wang, W. Ji, X. J. Zhou, et al., *Nat. Commun.* **2020**, *11*, 2453.
- [3] S. B. Desai, S. R. Madhvapathy, M. Amani, D. Kiriya, M. Hettick, M. Tosun, Y. Zhou, M. Dubey, J. W. Ager, D. Chrzan, A. Javey, *Adv. Mater.* **2016**, *28*, 4053.
- [4] G. Cabo, M. Michiardi, C. E. Sanders, M. Bianchi, D. Curcio, D. Phuyal, M. H. Berntsen, Q. Guo, M. I. Dendzik, *Adv. Sci.* **2023**, *10*, 2301243.
- [5] K. S. Novoselov, A. K. Geim, S. V. Morozov, D. Jiang, Y. Zhang, S. V. Dubonos, I. V. Grigorieva, A. A. Firsov, *Science* **2004**, *306*, 666.
- [6] X. Gao, L. Zheng, F. Luo, J. Qian, J. Wang, M. Yan, W. Wang, Q. Wu, J. Tang, Y. Cao, C. Tan, J. Tang, M. Zhu, Y. Wang, Y. Li, L. Sun, G. Gao, J. Yin, L. Lin, Z. Liu, S. Qin, H. Peng, *Nat. Commun.* **2022**, *13*, 5410.
- [7] L. Li, Q. Wang, F. Wu, Q. Xu, J. Tian, Z. Huang, Q. Wang, X. Zhao, Q. Zhang, Q. Fan, X. Li, Y. Peng, Y. Zhang, K. Ji, A. Zhi, H. Sun, M. Zhu, J. Zhu, N. Lu, Y. Lu, S. Wang, Bai, Y. Xu, W. Yang, N. Li, D. Shi, L. Xian, K. Liu, L. Du, G. Zhang, *Nat. Commun.* **2024**, *15*, 1825.
- [8] Q. Wang, N. Li, J. Tang, J. Zhu, Q. Zhang, Q. Jia, Y. Lu, Z. Wei, H. Yu, Y. Zhao, Y. Guo, L. Gu, G. Sun, W. Yang, R. Yang, D. Shi, G. Zhang, *Nano Lett.* **2020**, *20*, 7193.
- [9] Y. Chen, F. Fang, N. Zhang, *NPJ 2D Mater Appl* **2024**, *8*, 17.
- [10] T. Kang, T. W. Tang, B. Pan, H. Liu, K. Zhang, Z. Luo, *ACS Mater Au* **2022**, *2*, 665.
- [11] S. M. Hus, R. Ge, P. A. Chen, L. Liang, G. E. Donnelly, W. Ko, F. Huang, M. H. Chiang, A. P. Li, *Nat. Nanotech.* **2021**, *16*, 58.
- [12] F. Liu, W. Wu, Y. Bai, S. H. Chae, Q. Li, J. Wang, J. Hone, X. Y. Zhu, *Science* **2020**, *367*, 903.
- [13] K. Wu, H. Wang, M. Yang, L. Liu, Z. Sun, G. Hu, Y. Song, X. Han, J. Guo, K. Wu, B. Feng, C. Shen, Y. Huang, Y. Shi, Z. Cheng, H. Yang, L. Bao, S. T. Pantelides, H. J. Gao, *Adv. Mater.* **2024**, *36*, 2313511.
- [14] Y. Huang, Y. K. Wang, X. Y. Huang, G. H. Zhang, X. Han, Y. Yang, Y. Gao, L. Meng, Y. Wang, G. Z. Geng, L. W. Liu, L. Zhao, Z. H. Cheng, X. F. Liu, Z. F. Ren, H. X. Yang, Y. Hao, H. J. Gao, X. Y. Zhou, W. Ji, Y. L. Wang, *InfoMat* **2022**, *4*, e12274.
- [15] M. A. Islam, J. H. Kim, A. Schropp, H. Kalita, N. Choudhary, D. Weitzman, S. I. Khondaker, K. H. Oh, T. Roy, H. S. Chung, Y. Jung, *Nano Lett.* **2017**, *17*, 6157.
- [16] G. Zaborski Jr., P. E. Majchrzak, S. Lai, A. C. Johnson, A. P. Saunders, Z. Zhu, Y. Deng, D. Lu, M. Hashimoto, Z. X. Shen, F. Liu, Macroscopic uniform 2D moiré superlattices with controllable angles, <https://arxiv.org/pdf/2407.02600> (accessed: July 2024).
- [17] M. Bianchi, K. Hsieh, E. J. Porat, F. Dirnberger, J. Klein, K. Mosina, Z. Sofer, A. N. Rudenko, M. I. Katsnelson, Y. P. Chen, M. Rösner, P. Hofmann, *Phys. Rev. B* **2023**, *108*, 195410.
- [18] L. Pirker, J. Honolka, M. Velický, O. Frank, *2D Mater.* **2024**, *11*, 022003.
- [19] L. Guan, B. Xing, X. Niu, D. Wang, Y. Yu, S. Zhang, X. Yan, Y. Wang, J. Sha, *Chem. Commun.* **2018**, *54*, 595.
- [20] A. C. Johnston, S. I. Khondaker, *Adv. Mater. Interfaces* **2022**, *9*, 2200106.
- [21] J. Y. Moon, M. Kim, S.-I. Kim, S. Xu, J. H. Choi, D. Whang, K. Watanabe, T. Taniguchi, D. S. Park, J. Seo, S. H. Cho, S. K. Son, J. H. Lee, *Sci. Adv.* **2020**, *6*, eabc6601.
- [22] M. Velický, G. E. Donnelly, W. R. Hendren, W. J. I. DeBenedetti, M. A. Hines, K. S. Novoselov, H. D. Abruña, F. Huang, O. Frank, *Adv. Mater. Interfaces* **2020**, *7*, 2001324.
- [23] F. Liu, *Prog. Surf. Sci.* **2021**, *96*, 100626.
- [24] H. Sun, E. W. Sirott, J. Mastandrea, H. M. Gramling, Y. Zhou, M. Poschmann, H. K. Taylor, J. W. Ager, D. C. Chrzan, *Phys. Rev. Mater.* **2018**, *2*, 094004.
- [25] G. Pizzi, S. Milana, A. C. Ferrari, N. Marzari, M. Gibertini, *ACS Nano* **2021**, *15*, 12509.
- [26] X. Zhang, W. P. Han, J. B. Wu, S. Milana, Y. Lu, Q. Q. Li, A. C. Ferrari, P. H. Tan, *Phys. Rev. B* **2012**, *87*, 115413.
- [27] Y. Zhao, X. Luo, H. Li, J. Zhang, P. T. Araujo, C. K. Gan, J. Wu, H. Zhang, S. Y. Quek, M. S. Dresselhaus, Q. Xiong, *Nano Lett.* **2013**, *13*, 1007.
- [28] P. H. Tan, W. P. Han, W. J. Zhao, Z. H. Wu, K. Chang, H. Wang, Wang, N. Bonini, N. Marzari, N. Pugno, G. Savini, A. Lombardo, A. C. Ferrari, *Nat. Mater.* **2012**, *11*, 294.
- [29] M. Velický, A. Rodriguez, M. Bouša, A. V. Krayev, M. Vondráček, J. Honolka, M. Ahmadi, G. E. Donnelly, F. Huang, H. D. Abruña, K. S. Novoselov, O. Frank, *J. Phys. Chem. Lett.* **2020**, *11*, 6112.
- [30] S. L. Li, H. Miyazaki, H. Song, H. Kuramochi, S. Nakaharai, K. Tsukagoshi, *ACS Nano* **2012**, *6*, 7381.
- [31] H. Li, Q. Zhang, C. C. R. Yap, B. K. Tay, T. H. T. Edwin, A. Olivier, D. Baillargeat, *Adv. Funct. Mater.* **2012**, *22*, 1385.
- [32] D. Lloyd, X. Liu, J. W. Christopher, L. Cantley, A. Wadehra, B. L. Kim, B. B. Goldberg, A. K. Swan, J. S. Bunch, *Nano Lett.* **2016**, *16*, 5836.
- [33] A. Michail, N. Delikoukos, J. Parthenios, C. Galiotis, K. Papagelis, *Appl. Phys. Lett.* **2016**, *108*, 173102.
- [34] H. J. Conley, B. Wang, J. I. Ziegler, R. F. Haglund, S. T. Pantelides, K. I. Bolotin, *Nano Lett.* **2013**, *13*, 3626.
- [35] T. Peña, S. A. Chowdhury, A. Azizimanesh, A. Sewaket, H. Askari, S. M. Wu, *2D Mater.* **2021**, *8*, 045001.
- [36] G. Kukulcska, J. Koltai, *Phys. Status Solidi B* **2017**, *254*, 1700184.
- [37] B. Chakraborty, A. Bera, D. V. S. Muthu, S. Bhowmick, U. V. Waghmare, A. K. Sood, *Phys. Rev. B* **2012**, *85*, 161403.
- [38] X. Huang, L. Zhang, L. Liu, Y. Qin, Q. Fu, Q. Wu, R. YANG, J. P. LV, Z. Ni, L. Liu, W. Ji, Y. Wang, X. Zhou, Y. Huang, *Sci. China Inf. Sci.* **2021**, *64*, 140406.
- [39] J. Van Baren, G. Ye, J. A. Yan, Z. Ye, P. Rezaie, P. Yu, Z. Liu, R. He, C. H. Lui, *2D Mater.* **2019**, *6*, 025022.
- [40] E. Khestanova, F. Guinea, L. Fumagalli, A. K. Geim, I. V. Grigorieva, *Nat. Commun.* **2016**, *7*, 12587.
- [41] Y. Kim, P. Herlinger, T. Taniguchi, K. Watanabe, J. H. Smet, *ACS Nano* **2019**, *13*, 14182.
- [42] M. Zhao, C. Casiraghi, K. Parvez, *Chem. Soc. Rev.* **2024**, *53*, 3036.
- [43] P. Ci, Y. Chen, J. Kang, R. Suzuki, H. S. Choe, J. Suh, C. Ko, T. Park, K. Shen, Y. Iwasa, S. Tongay, J. W. Ager, L. W. Wang, J. Wu, *Nano Lett.* **2017**, *17*, 4982.
- [44] P. Giannozzi, S. Baroni, N. Bonini, M. Calandra, R. Car, C. Cavazzoni, D. Ceresoli, G. L. Chiarotti, M. Cococcioni, I. Dabo, A. Dal Corso, S. De Gironcoli, S. Fabris, G. Fratesi, R. Gebauer, U. Gerstmann, C. Gougoussis, A. Kokalj, M. Lazzeri, L. Martin-Samos, N. Marzari, F. Mauri, R. Mazzarello, S. Paolini, A. Pasquarello, L. Paulatto, C. Sbraccia, S. Scandolo, G. Sclauzero, A. P. Seitsonen, et al., *J. Phys. Cond. Matt.* **2009**, *21*, 395502.
- [45] P. Giannozzi, O. Andreussi, T. Brumme, O. Bunau, M. Buongiorno Nardelli, M. Calandra, R. Car, C. Cavazzoni, D. Ceresoli, M. Cococcioni, N. Colonna, I. Carnimeo, A. Dal Corso, S. De Gironcoli,

- P. Delugas, R. A. Distasio, A. Ferretti, A. Floris, Fratesi, G. Fugallo, R. Gebauer, U. Gerstmann, F. Giustino, T. Gorni, J. Jia, M. Kawamura, H. Y. Ko, A. Kokalj, E. Küçükbenli, M. Lazzeri, et al., *J. Phys. Cond. Matt.* **2017**, 29, 465901.
- [46] A. Dal Corso, *Comput. Mater. Sci.* **2014**, 95, 337.
- [47] J. P. Perdew, K. Burke, M. Ernzerhof, *Phys. Rev. Lett.* **1996**, 77, 3865.
- [48] H. J. Monkhorst, J. D. Pack, *Spec. Point. Brillouin-Zone Integrat.* **1976**, 13, 5188.
- [49] S. R. Billeter, A. J. Turner, W. Thiel, *Phys. Chem. Chem. Phys.* **2000**, 2, 2177.
- [50] S. Grimme, J. Antony, S. Ehrlich, H. Krieg, *J. Chem. Phys.* **2010**, 132, 154104.
- [51] K. Momma, F. Izumi, *J. Appl. Crystallogr.* **2011**, 44, 1272.